

# Towards Frequency-Adaptive Learning for SAR Despeckling

Ziqing Ma, Chang Yang, Zhichang Guo, Yao Li

**Abstract**—Synthetic Aperture Radar (SAR) images are inherently corrupted by speckle noise, limiting their utility in high-precision applications. While deep learning methods have shown promise in SAR despeckling, most methods employ a single unified network to process the entire image, failing to account for the distinct speckle statistics associated with different spatial physical characteristics. It often leads to artifacts, blurred edges, and texture distortion. To address these issues, we propose SAR-FAH, a frequency-adaptive heterogeneous despeckling model based on a divide-and-conquer architecture. First, wavelet decomposition is used to separate the image into frequency sub-bands carrying different intrinsic characteristics. Inspired by their differing noise characteristics, we design specialized sub-networks for different frequency components. The tailored approach leverages statistical variations across frequencies, improving edge and texture preservation while suppressing noise. Specifically, for the low-frequency part, denoising is formulated as a continuous dynamic system via neural ordinary differential equations, ensuring structural fidelity and sufficient smoothness that prevents artifacts. For high-frequency sub-bands rich in edges and textures, we introduce an enhanced U-Net with deformable convolutions for noise suppression and enhanced features. Extensive experiments on synthetic and real SAR images validate the superior performance of the proposed model in noise removal and structural preservation.

**Index Terms**—Synthetic Aperture Radar, frequency adaptive, wavelet transform, structural preservation, neural ordinary differential equations

## I. INTRODUCTION

Synthetic Aperture Radar (SAR) is an all-weather, high-resolution coherent imaging sensor that captures terrain backscatter to produce images. Due to its unique imaging capabilities, SAR is widely used in military reconnaissance, terrain mapping, disaster monitoring, and various other applications [1], [2]. However, the coherent interference of waves introduces speckle noise, a type of signal-dependent granular noise that typically manifests as bright or dark spots in the images. This strong coherence significantly disrupts image structures, making it difficult to perform downstream tasks such as segmentation [3], recognition [4], and classification [5]. Thus, speckle noise removal, also known as despeckling, while preserving important structures in SAR images, is a challenging but significant task.

Designing effective speckle reduction methods remains challenging due to the need to balance noise suppression with structural preservation. In recent years, deep learning approaches using convolutional neural networks (CNNs) have significantly advanced SAR despeckling by learning end-to-end mappings from noisy to clean images [6], [8], [9]. For

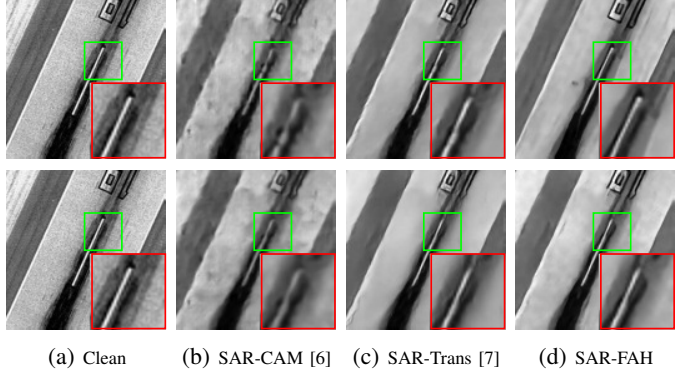


Fig. 1: The illustration of restored results obtained by state-of-the-art methods using different training dataset. The first row is trained on a synthetic SAR dataset, while the second row is trained on a texture dataset. It demonstrates that increasing texture richness in the dataset helps with texture preservation.

instance, Chierchia et al. [8] adopted a homomorphic strategy with DnCNN [10] for additive noise removal, yet struggled in real SAR scenarios. Zhang et al. [9] improved upon this by learning direct non-linear mappings and incorporating dilated convolutions to expand receptive fields. Further enhancements include Ko et al. [6], who integrated attention mechanisms and total variation loss for textural preservation, and Thakur et al. [11], who combined attention mechanism and gradient features to extract finer details. Additionally, Perera et al. [7] employed transformers to capture global dependencies, further improving texture and detail recovery.

Although existing methods have improved structural preservation in SAR despeckling, a key limitation persists. CNNs are inherently biased toward statistically dominant features [12], enabling a bias of heterogeneous features. In such cases, the model does indeed result in blurred edges and texture distortion in the restored results, as shown in the first row of figure 1. To address this limitation and enhance texture protection, adding images with rich heterogeneous features, like texture, to the dataset for training can improve its preservations to some extent. As shown in the second row of figure 1, the SAR-CAM [6] and the SAR-Trans [7] trained on texture datasets can alleviate reduces the blurring of edges. However, due to the limited heterogeneous features in natural images, this improvement is constrained.

On the other hand, these networks aim to implicitly learn the statistical distribution of speckle noise. However, SAR images can be divided into homogeneous and heterogeneous regions. Commonly, speckle noise in homogeneous areas, including structures such as sea surface and roads, conforms to the assumption of sufficient development and usually follows the

Corresponding author: Zhichang Guo (e-mail: mathgzc@hit.edu.cn)

Ziqing Ma, Chang Yang, Zhichang Guo, and Yao Li are with the School of Mathematics, Harbin Institute of Technology, Harbin 150001, China. (e-mail: 23b912037@stu.hit.edu.cn, yangchang@hit.edu.cn, mathgzc@hit.edu.cn, yaoli0508@hit.edu.cn)

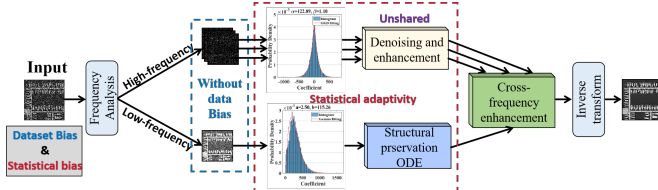


Fig. 2: The framework of the proposed SAR-FAH model.

square root of Gamma distribution [13]. Inversely, the heterogeneous regions often capture strong scatterers to produce tree, frost, and other isolated targets, exhibiting distinct noise distributions due to the signal-dependent nature of speckle. They are typically modelled as  $K$ -distribution [13], respectively. Most deep learning approaches, however, rely on a unified model, implicitly earning the "average" or "compromise" of all possible statistical characteristics encountered resulting in artifacts in homogeneous regions or blurred structures in heterogeneous regions. For solving this limitations, Vitale et al. [14] designed a multi-objective cost function by considering the spatial and statistical properties of SAR image. They minimized the statistical difference between the estimated ratio image and theoretical fully developed speckle to consider the statical property of speckle noise. Besides, gradient was employed for edge and strong scatterers preservation. Yu et al. [15] proposed a collaborative optimization model by incorporating structure extraction module to extract heterogeneous features and weighting structural loss function to protect edges and textural details. However, they did not completely separate the regional-related noise to sufficiently utilize different spatially statistical characteristics, resulting in suboptimal recovery results.

To tackle these challenges, we propose a frequency-adaptive heterogeneous network, called SAR-FAH, to balance noise suppression and structural protection. The overall framework is shown in figure 2. For address dataset bias and fully utilize the statistical differences of different characteristic regions, frequency analysis is used to decouple regions with different physical characteristics enabling sufficient utilization statistical difference. Upon these, we design a heterogeneous network to process low-frequency and high-frequency, respectively. To avoid artifacts and structural loss, and based on the smoothness of the process, we employ neural ordinary differential equations (NODEs) framework to construct a low-frequency denoising network that controls the smooth evolution of low-frequency features under the control of the dynamic system, ensuring sufficient smoothness and structural fidelity. For high-frequency domains, multi-scale extractions and deformable convolutions are used to extract edges and textures for denoising and structural enhancement. Through frequency-adaptive learning, the proposed SAR-FAH model achieves better despeckling performance, as shown in figure 1d, with clear image structures.

The main contributions of this work are as follows:

- 1) We propose a SAR-FAH model to effectively balance noise suppression and structural preservation. Due to the impact of the frequency bias of the dataset on the

training results of the network, we adopt a separation strategy to perform frequency analysis on the dataset and input it into the network for divide-and-conquer processing.

- 2) We employ wavelet transform to decompose the SAR image into high- and low-frequency components, enabling explicit analysis of the distinct statistical properties of speckle noise in different regions. Furthermore, We design a specialized noise removal module to adaptively learn the statistical characteristics of noise at different frequencies, enhancing structural retention during noise removal.
- 3) A low-frequency structural preservation-ODE (LFSP-ODE) module is designed for enhance the fidelity of image structures based on NODE framework. The module allows adequate smoothness and the controlled evolution of noisy low-frequency features, enabling enhanced structural fidelity without artifacts.
- 4) For the high-frequency components, which contain significant sharp edges and textures, we design a high-frequency denoising and enhancement (HFDE) module based on a U-Net architecture. It extracts multi-scale features and incorporates deformable convolutions to adaptively capture boundaries and fine textures, thereby enhancing high-frequency structures during the denoising process.

The remainder of this paper is structured as follows. Section II reviews related work on SAR despeckling. Section III details the proposed methodology including our contributions. Section V presents experimental results on synthetic SAR images, textural images, and real SAR datasets. Finally, we concludes in section VI.

## II. RELATED WORK

### A. Deep-learning SAR despeckling methods

Advances in computing have driven the widespread adoption of deep learning in SAR despeckling. For instance, Chierchia et al. [8] combined logarithmic and exponential transformations to convert SAR despeckling into an additive noise removal task solving by DnCNN [10]. Different this transform, Wang et al. [16] employed similar network to estimate speckle noise, and combined total variation loss for end-to-end training enabling the preservation of edges. Furthermore, Zhang et al. [9] applied dilated convolution and residual networks to enlarge the receptive field and mitigate the vanishing gradient problem in despeckling tasks.

Despite proficient noise suppression, existing CNN-based despeckling methods frequently exhibit suboptimal preservation of image structures including blurred edges and loss of texture. To bridge this gap, subsequent research has introduced more sophisticated architectures. Ko et al. [6] integrated an attention mechanism [17] to refine features contextually, improving texture preservation. Liu et al. [18] decomposed the image via wavelet transform, using attention to suppress noise in frequency sub-bands, complemented by multi-scale feature extraction for structural enhancement. Additionally, Li et al.

[19] embedded multi-scale extraction within a U-shape framework for structural similar enhancement. To explicitly guide the network in preserving edges, Thakur et al. [11] augmented features with gradient information to sharpen edges. Acknowledging the fundamental limitation of the local receptive field of CNNs, Perera et al. [7] introduced a transformer-based model, leveraging self-attention to capture long-range dependencies and generating high-resolution details as well as low-resolution coarse structures.

Nevertheless, the aforementioned approaches overlook the inherent statistical properties in homogeneous and heterogeneous regions, often leading to artifacts or distorted textures as well as compromised isolated targets. In response, Vitale et al. [14] formulated a multi-objective loss function aimed at preserving statistical properties on homogeneous regions, textures, and edges simultaneously. More recently, Yu et al. [15] utilized a pre-trained edge detection network to extract heterogeneous features, providing structural supervision by collaborative optimization. Despite these efforts, they still fail to fully exploit the spatial statistical heterogeneity of SAR images, primarily due to the challenge of segmenting regions with distinct physical characteristics.

### B. NODE for structural fidelity

While residual networks have enabled the construction of deeper architectures for stronger feature extraction, their inherently discrete block-by-block processing often leads to structural degradation and a rapid explosion in parameter count, which fundamentally limits their effectiveness in SAR despeckling tasks. To overcome these limitations, Neural Ordinary Differential Equations (NODE) [20] present a compelling alternative by modelling feature evolution through a continuous dynamical system, which has shown promising results in related image restoration tasks [21], [22]. It is expressed as follows:

$$\frac{d\mathbf{u}(\omega)}{dt} = \mathcal{N}_\theta(\mathbf{u}(t), t), \quad t \in (0, T], \quad (1)$$

$$\mathbf{u}(0) = \mathbf{f},$$

where the function  $\mathcal{N}_\theta$  parameterizes the time derivative of the hidden state  $\mathbf{u}(t)$  using a neural network, learning the continuous dynamics that govern the feature evolution. It inherits advantageous properties of ODE solutions, ensuring structural fidelity. In practice, the system is discretized and solved numerically using an ODE solver. As the complexity of the network increases, the parameter count remains unchanged. On the contrary, with the number of times solved by the ODE solver, the accuracy of the solution continues to improve with increased computational complexity obtaining better parameter utilization.

### C. VMamba for global feature extraction

Global feature extraction plays a crucial role in preserving textural structures in visual data. While transformer-based models excel at capturing global contextual information, their computational complexity increases quadratically with sequence length, hindering practical scalability. To overcome this limitation, Liu et al. [23] introduced vision mamba (VMamba),

a model built upon the Mamba framework [24], which enables efficient long-range dependency modelling with linear computational complexity. Its efficiency has proven beneficial across various image processing tasks [25]–[27]. VMamba incorporates a 2-dimensional (2D) selective scanning (SS2D) mechanism, which converts image data into 1D sequences. These sequences are then processed by a selective state space model (SSM) [28] to capture global dependencies. The model subsequently applies a weighting mechanism to reconstruct the 2D structural information from the outputs. The SSM maps a 1D input sequence  $x(s) \in \mathbb{R}$  to an output  $y(s) \in \mathbb{R}$  via a hidden state  $\mathbf{h}(s) \in \mathbb{R}^L$ , where  $L$  denotes the hidden state dimension, respectively. The continuous-time SSM is described by a linear ODE system:

$$\mathbf{h}'(s) = \mathbf{A}\mathbf{h}(s) + \mathbf{B}x(s), \quad y(s) = \mathbf{C}\mathbf{h}(s) + \mathbf{D}x(s),$$

where  $\mathbf{A} \in \mathbb{R}^{L \times L}$  and  $\mathbf{D} \in \mathbb{R}$  are learnable parameters, while  $\mathbf{B} \in \mathbb{R}^{L \times 1}$  and  $\mathbf{C} \in \mathbb{R}^{1 \times L}$  are derived from the input  $x(s)$ . To integrate this system into deep learning frameworks, the continuous-time model is discretized using a learnable timescale parameter  $\Delta \in \mathbb{R}^{L \times L}$ . Applying the Zero-Order Hold method [29] yields the discrete form:

$$\bar{\mathbf{A}} = e^{\Delta \mathbf{A}}, \quad \bar{\mathbf{B}} = (\Delta \mathbf{A})^{-1} (e^{\Delta \mathbf{A}} - \mathbf{I}) \cdot \Delta \mathbf{B}, \quad (2)$$

$$\mathbf{h}_s = \bar{\mathbf{A}}\mathbf{h}_{s-1} + \bar{\mathbf{B}}x_s, \quad y_s = \mathbf{C}\mathbf{h}_s + \mathbf{D}x_s.$$

## III. METHODOLOGY

### A. The analysis of dataset bias

Most existing deep learning-based despeckling models are data-driven, and their performance depends on both feature extraction capability of the model and the construction of the training dataset. However, many current models often suffer from artifacts, edge blurring, and texture distortion after noise suppression.

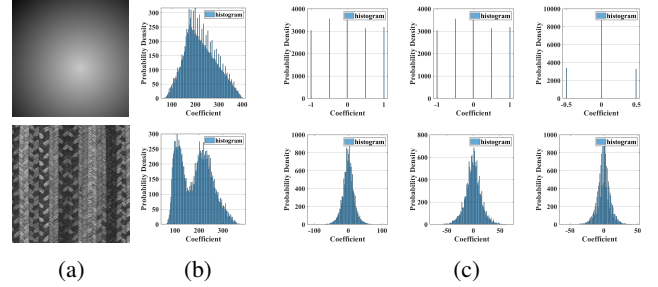


Fig. 3: Energy analysis of gradient-dominated image (first row) and texture-rich image (second row). It illustrates the homogeneous bias in dataset. (a) shows the original image. The energy distribution are shown in (b) for homogeneous regions, and (c) for heterogeneous regions.

To investigate the underlying cause, we firstly analyse it from the perspective of dataset. SAR images can be broadly categorized into homogeneous and heterogeneous regions based on local spatial characteristics. Usually, there is a significant difference in the proportion of these two parts in the image. We selected a gradient-dominated image with mostly homogeneous areas and a texture-rich image, as shown

in figure 3a, to analyse the region distribution. As shown in figure 3b and 3c, the distribution histograms of pixel values reveal that homogeneous regions contain significantly more pixels than heterogeneous regions in both images. Therefore, homogeneous regions often dominate highly in natural images.

Deep learning models, as data-fitting tools that minimize a global loss function via gradient descent, inherently tend to fit the majority of samples during training to rapidly reduce overall loss [12]. Consequently, given the numerical dominance of homogeneous pixels in a datasets, the optimization of the model naturally prioritizes fitting these regions, leading to insufficient learning of edges and textures in heterogeneous areas, ultimately causing blurring and distortion in despeckling results.

Unfortunately, despite the richness of natural images, their textural structures are inherently limited as mentioned above. Rather than modifying the dataset itself, we propose to adjust how the model processes data to correct inherent learning biases. Our solution is to integrate wavelet decomposition, specifically using the 2D separable Haar wavelet. Grounded in multi-resolution analysis theory [30] for  $L^2(\mathbb{R}^2)$ , this approach projects an image onto different orthogonal subspaces. This effectively separates features and elevates them to equal importance, thereby solving the problem of imbalanced distribution. Specifically, the image is decoupled into four physically distinct subspaces: one low-frequency subspace that captures information from homogeneous regions, and three high-frequency subspaces that focus on heterogeneous, directionally-oriented features. This decomposition creates a more balanced feature learning process, encouraging the model to perform comprehensive restoration across all image regions.

### B. Frequency analysis and statistical property study

Speckle noise in SAR images is typically modelled as multiplicative noise. Under the well-developed hypothesis, it follows a Gamma distribution, denoted by  $\mathcal{GM}$ , characterized by the probability density function:

$$p(x,a,b) = \frac{b^{-a}}{\Gamma(a)} x^{a-1} \exp(-\frac{x}{b}) \chi_{\{x \geq 0\}},$$

where  $\chi$  is the indicator function,  $a$  is shape parameter, and  $b$  is scale parameter. Usually, it is supposed that mean  $ab$  is equal to 1, and the variance if  $ab^2 = L$ , where  $L$  is number of looks.

However, in heterogeneous regions containing strong scatterers, the conditions for fully developed speckle are often not satisfied. As a result, these regions are better characterized by a  $K$ -distribution [13]. This divergence in statistical characteristics between homogeneous and heterogeneous areas poses a significant challenge for denoising models. A single, unified model struggles to accommodate both statistical regimes effectively, leading to a problematic "compromise" in a single complex mapping task. Typically, such a model faces a dilemma: if it focuses on fully suppressing noise, excessive smoothing tends to blur edges and distort textures; conversely, if it prioritizes preserving structural features in heterogeneous regions, its limited smoothing ability often leaves substantial

residual noise and artifacts in uniform areas. The fundamental issue is that these two regions are often spatially intertwined, preventing existing models from fully leveraging their inherent statistical differences and thereby limiting overall denoising performance.

Fortunately, by using Haar wavelet decomposition, beyond resolving dataset bias, it offers a decisive solution to the core challenge outlined above, which completely separates homogeneous and heterogeneous regions in the frequency domain. This critical separation enables to fully exploiting inherent statistical differences. The 2D separable Haar wavelet bias filters are defined as:

$$\begin{aligned} \omega^{LL} &= \frac{1}{2} \begin{bmatrix} 1 & 1 \\ 1 & 1 \end{bmatrix}, \quad \omega^{LH} = \frac{1}{2} \begin{bmatrix} -1 & -1 \\ 1 & 1 \end{bmatrix}, \\ \omega^{HL} &= \frac{1}{2} \begin{bmatrix} -1 & 1 \\ -1 & 1 \end{bmatrix}, \quad \omega^{HH} = \frac{1}{2} \begin{bmatrix} 1 & -1 \\ -1 & 1 \end{bmatrix}. \end{aligned} \quad (3)$$

Then the homogeneous region is projected in low-frequency sub-band using  $\omega^{LL}$ , while the heterogeneous parts are put into high-frequency sub-bands in three directions based on  $\{\omega^{LH}, \omega^{HL}, \omega^{HH}\}$ . After such decomposition, the spatial differences in the noise of SAR images are transformed into frequency domain differences. And through the theorem 1 referred to [31], we have thoroughly studied the statistical distribution of coefficients in different frequency domains.

**Theorem 1.** *Let  $\mathbf{X} = \{x[m, n]\}$  be an image of size  $2^J \times 2^J$ , where  $x[m, n]$  are independent and identically distributed random variables following the Gamma distribution  $\mathcal{GM}(a, b)$ . Consider the 2D multi-resolution analysis of  $\mathbf{X}$  using 2D separable orthonormal Haar wavelets. Then the wavelet coefficients at scale  $j$  exhibit the following properties:*

- 1) *The low-frequency coefficients (LL sub-band)  $\mathbf{A}_j(k, l)$  at scale  $j$  follow a Gamma distribution:*

$$\mathbf{A}_j(k, l) \sim \mathcal{GM}(2^{2j}a, 2^{-j}b),$$

*where  $1 \leq k, l \leq 2^{J-j}$ .*

- 2) *The high-frequency coefficients (LH, HL, and HH sub-bands)  $\mathbf{D}_j^i(k, l)$  at scale  $j$  follow a symmetric distribution, where  $i = LH, HL, HH$  and  $1 \leq k, l \leq 2^{J-j}$ .*

*Proof.* For the 2D image, we use wavelet bias in (3) to decompose it into low-frequency  $\mathbf{A}_j$  and high-frequency coefficients  $\mathbf{D}_j^i$  at the scale  $j$  as follows:

$$\begin{aligned} \mathbf{A}_j(k, l) &= \sum_{m=1}^2 \sum_{n=1}^2 \omega^{LL}(m, n) \mathbf{A}_{j-1}[2k-m, 2l-n], \\ \mathbf{D}_j^i(k, l) &= \sum_{m=1}^2 \sum_{n=1}^2 \omega^i(m, n) \mathbf{A}_{j-1}[2k-m, 2l-n]. \end{aligned}$$

At the first decomposition level, it is directly to calculate that:

$$\mathbf{A}_1(k, l) = \frac{1}{2} \sum_{m=1}^2 \sum_{n=1}^2 x[2k-m, 2l-n].$$

According to the properties of Gamma distribution, it follows that  $\mathbf{A}_1(k, l) \sim \mathcal{GM}(2^2a, 2^{-1}b)$ .

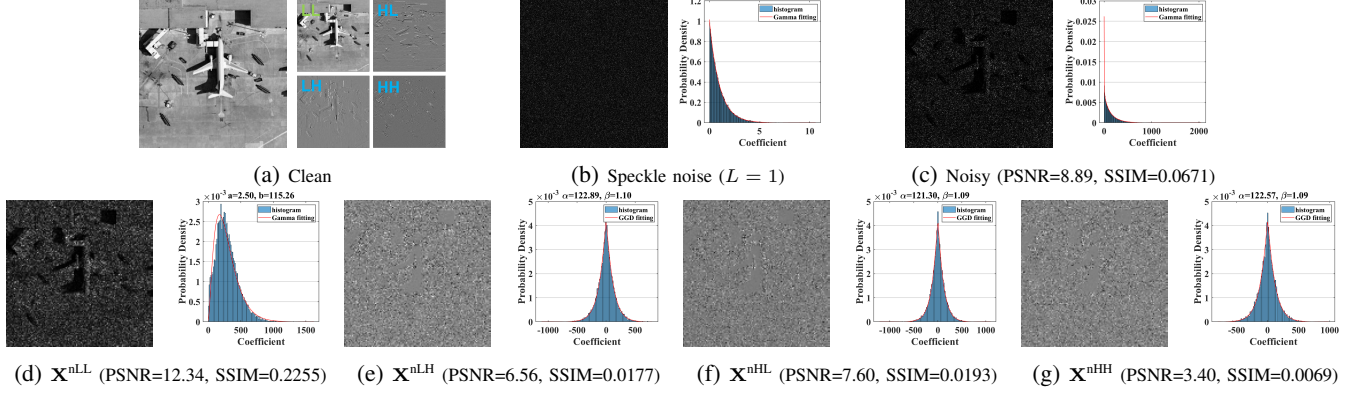


Fig. 4: Synthetic texture images disrupted by speckle noise ( $L = 1$ ) to study statistical property after wavelet decomposition. (a) Clean SAR image and its decomposition by 2D Haar wavelet transform. (b) - (g) show the speckle noise ((b)), noisy image ((c)), low-frequency sub-band  $X^{nLL}$  ((d)), low-frequency sub-band  $X^{nLH}$  ((e)),  $X^{nHL}$  ((f)),  $X^{nHH}$  ((g)), with their histogram fitting by  $\mathcal{GM}$  and  $\mathcal{GGD}$  distribution, respectively. We also label the PSNR, SSIM value, and fitting parameters.

At the second decomposition level, we have:

$$\mathbf{A}_2(k, l) = \frac{1}{2} \sum_{m=1}^2 \sum_{n=1}^2 \mathbf{A}_1[2k - m, 2l - n].$$

By the same ways, one gets that  $\mathbf{A}_2(k, l) \sim \mathcal{GM}(2^4 a, 2^{-2} b)$ . Therefore, at the  $j$ -th decomposition level, we conclude that  $\mathbf{A}_j(k, l) \sim \mathcal{GM}(2^{2j} a, 2^{-j} b)$ .

The high-frequency coefficient  $\mathbf{D}_1^{HH}(k, l)$  is calculated as

$$\mathbf{D}_j^{HH}(k, l) = \frac{1}{2} (\mathbf{A}_{j-1}[2k-1, 2l-1] - \mathbf{A}_{j-1}[2k-2, 2l-1] - \mathbf{A}_{j-1}[2k-1, 2l-2] + \mathbf{A}_{j-1}[2k-2, 2l-2])$$

at the first decomposition level. As above-mentioned, one has

$$\frac{1}{2} (\mathbf{A}_{j-1}[2k-1, 2l-1] + \mathbf{A}_{j-1}[2k-2, 2l-2]) \sim \mathcal{GM}(2^{2j} a, 2^{-j} b)$$

and

$$\frac{1}{2} (\mathbf{A}_{j-1}[2k-2, 2l-1] + \mathbf{A}_{j-1}[2k-1, 2l-2]) \sim \mathcal{GM}(2^{2j} a, 2^{-j} b).$$

In this way, the distribution of  $\mathbf{D}_j^{HH}(k, l)$  follows a Gamma difference distribution [32], which has the probability density function as follows:

$$f(z) = \begin{cases} \frac{\tilde{b}^{2\tilde{a}}}{\Gamma(\tilde{a})^2} e^{-\tilde{b}z} \int_z^\infty x^{\tilde{a}-1} (x-z)^{\tilde{a}-1} e^{-2\tilde{b}x} dx, & z > 0, \\ \frac{\tilde{b}^{2\tilde{a}}}{\Gamma(\tilde{a})^2} e^{-\tilde{b}z} \int_{-z}^\infty x^{\tilde{a}-1} (x+z)^{\tilde{a}-1} e^{-2\tilde{b}x} dx, & z < 0 \end{cases}$$

where  $\tilde{a} = 2^{2j} a$  and  $\tilde{b} = 2^{-j} b$ . It is clearly that  $f(z)$  is symmetric centered in zero. In addition, based on same derivation, we can conclude that all high-frequency coefficients  $\mathbf{D}_j^i$  follow a symmetric distribution.  $\square$

A SAR image corrupted by speckle noise with  $L = 1$  is used as an illustrative example, as shown in figure 4. In this work, we only decompose the SAR image at scale of  $j = 1$  for efficient implementation. When clean SAR images are decomposed via the Haar wavelet transform, they exhibit distinct characteristics across four different sub-spaces. However, when corrupted by speckle noise, most image structures become obscured, and the entire image can be closely

approximated by a  $\mathcal{GM}(0.87, 167.89)$  distribution. Although the spatial statistical distributions vary, their visual manifestations remain difficult to interpret. By applying wavelet transform for frequency-domain analysis, we fully decouple the spatially mixed features, revealing statistical differences in noise, arising from different spatial physical characteristics, across different frequency sub-bands. As consistent with theorem 1, the low-frequency region is well characterized by  $\mathcal{GM}(2.50, 115.26)$ , while we use the generalized Gaussian distribution, denoted by  $\mathcal{GGD}$ , to model the high-frequency sub-bands. The probability density function of the  $\mathcal{GGD}$  is given by:

$$g(x, \alpha, \beta) = \frac{\beta}{2\alpha\Gamma(1/\beta)} e^{-(\frac{|x|}{\alpha})^\beta},$$

where  $\alpha, \beta > 0$  represents scale and shape parameter, respectively. As shown in figure 4, the high-frequency features follow  $\mathcal{GGD}(122.89, 1.10)$ ,  $\mathcal{GGD}(121.30, 1.09)$ ,  $\mathcal{GGD}(122.57, 1.09)$ , respectively. These distributional differences allow clear separation of regions with distinct physical and statistical properties, motivating the design of adaptive denoising networks tailored to different sub-bands.

Additionally, it is noteworthy that wavelet decomposition effectively separates noise from structural content, providing further advantages for structure preservation. Although the high-frequency components collectively follow the same type of distribution, their parameters differ. Moreover, high-frequency structures and the degree of noise contamination vary across directional sub-bands, as reflected in the differing PSNR and SSIM values presented in figure 4. To accommodate such statistical variations, we use same but unshared modules ensuring better adaptation for high-frequency processing.

#### IV. THE PROPOSED METHOD

##### A. Overall network structures

The proposed SAR-FAH model employs a four-branch architecture that adaptively processes features from different frequency bands using dedicated modules, as shown in figure 2. It comprises three core components: a Low-Frequency

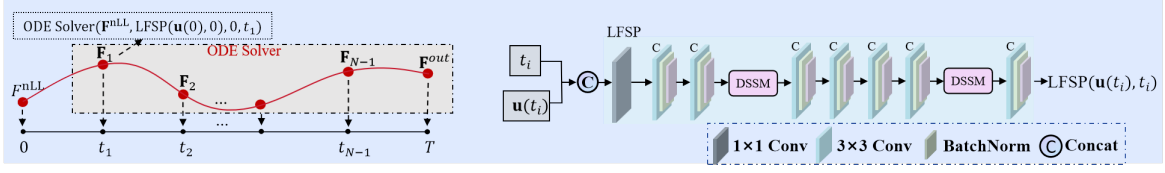


Fig. 5: Low-frequency structural preservation-ODE (LFSP-ODE) module.

Structural Preservation-ODE (LFSP-ODE) module, a High-Frequency Denoising and Enhancement (HFDE) module, and a Cross-Frequency enhancement (CFRE) module. The LFSP-ODE module is based on NODE framework, modelling low-frequency denoising and structural preservation as a continuous dynamical system. The HFDE module adopts an asymmetric U-shaped design inspired by U-Net [33], enabling multi-scale feature extraction and adaptive processing of irregular edges to preserve sharp structures and texture details in high-frequency components. The CFRE facilitates interactive feature fusion between the processed low- and high-frequency components, guiding the structural-coherent restoration of the full image.

Given a noisy SAR image  $\mathbf{X}^n \in \mathbb{R}^{1 \times H \times W}$ , a 2D discrete Haar wavelet transform decomposes it into one low-frequency component  $\mathbf{X}^{nLL}$  and three high-frequency components  $\{\mathbf{X}^{nLH}, \mathbf{X}^{nHL}, \mathbf{X}^{nHH}\}$ . Each component has dimensions  $\mathbb{R}^{1 \times \frac{H}{2} \times \frac{W}{2}}$ . Then a  $3 \times 3$  convolution then projects them into a higher-dimensional feature space, yielding  $\mathbf{F}^{nLL}, \mathbf{F}^{nLH}, \mathbf{F}^{nHL}, \mathbf{F}^{nHH} \in \mathbb{R}^{C \times \frac{H}{2} \times \frac{W}{2}}$ , with  $C$  denoting the number of feature channels. The low-frequency feature  $\mathbf{F}^{nLL}$  is processed by the LFSP-ODE module, while the high-frequency features are independently denoised and enhanced by the HFDE module, producing denoised features  $\mathbf{F}^{LL}, \mathbf{F}^{LH}, \mathbf{F}^{HL}, \mathbf{F}^{HH} \in \mathbb{R}^{C \times \frac{H}{2} \times \frac{W}{2}}$ . Then they are fed into CFRE module for structural enhancement. Specially, these features are concatenated along the channel dimension and fused via a  $1 \times 1$  convolution to enable cross-band interaction and structural-coherent restoration. A residual blocks then helps preserve information, resulting in a composite feature  $\mathbf{F} \in \mathbb{R}^{4C \times \frac{H}{2} \times \frac{W}{2}}$ . Finally, the image is reconstructed using the inverse wavelet transform to obtain  $\mathbf{X}^{out} \in \mathbb{R}^{1 \times H \times W}$ .

Given a training set of noisy-clean image pairs  $\{\mathbf{X}_i^n, \mathbf{X}_i\}$ , the model is optimized using the  $L_1$  loss function:

$$\mathcal{L}(\Theta) = \frac{1}{n} \sum_{i=1}^n \| f_{\text{SAR-FAH}}(\mathbf{X}_i^n; \Theta) - \mathbf{X}_i \|_1,$$

where  $\Theta$  denotes the learnable parameters.

#### B. Low-frequency structural preservation-ODE module

In SAR speckle reduction, it is important to note that the low-frequency part may produce artifacts due to insufficient smoothing or result in structural loss during the denoising process. In order to completely smooth out noise while preserving the complete image structure of the output image for low-frequency feature input, a high degree of similarity between the input and output is required, which can be expressed as a controllability problem of the dynamic system.

And the processing at the low frequency is a sufficiently smooth problem, as there is a mapping generated by ODE that corresponds to this process [34], [35]. In this way, we construct LFSP-ODE module, which incorporates denoising of low-frequency regions into the NODE framework [20], allowing features to undergo continuous transformations through hidden layers under the control of ODE. By modelling the process as a continuous dynamical system controlled by ODE, it mitigates information loss and artifacts due to the dependence of the solution on the initial value and the regularity of the solution [36].

Guided by the dynamical system perspective in equation (1), we formulate the feature denoising process for the low-frequency component as a continuous-time evolution. This process is described by the following initial value problem defined over the temporal domain  $t \in (0, T]$ :

$$\begin{aligned} \frac{d\mathbf{u}(t)}{dt} &= f_{\theta}^{\text{LFSP}}(\mathbf{u}(t), t), \quad t \in (0, T], \\ \mathbf{u}(0) &= \mathbf{F}^{nLL}, \end{aligned}$$

where  $\mathbf{u}(t)$  represents the latent feature state at time  $t$ . To solve this problem numerically, we discretize the temporal domain and derive the update rule:

$$\begin{aligned} \mathbf{u}(t_{i+1}) &= \mathbf{u}(t_i) + \int_{t_i}^{t_{i+1}} f_{\theta}^{\text{LFSP}}(\mathbf{u}(t), t) dt, \\ &= \text{ODESolver}(\mathbf{u}(t_i), f_{\theta}^{\text{LFSP}}, t_i, t_{i+1}), \end{aligned} \quad (4)$$

with  $0 = t_0 \leq t_1 \leq \dots \leq t_N = T$  and a step size  $t_{i+1} - t_i = \frac{T}{N}$ . Here, ODESolver is implemented using a randomized Euler method. The final state  $\mathbf{u}(T)$  corresponds to the denoised low-frequency feature  $\mathbf{F}^{LL}$ .

The vector field  $f_{\theta}^{\text{LFSP}}$ , parameterized by the LFSP module, maps the input  $\mathbf{u}(t_i)$  concatenated with  $t_i$  to an output of the same dimension as  $\mathbf{u}(t_i)$ . The LFSP architecture comprises 7 Conv-BN-ReLU denoising blocks, augmented by two DASS modules that enhance denoising through dynamic integration of global and local features using a hybrid of VMamba and attention mechanisms.

The LFSP-ODE module contributes to improved structural fidelity in the denoising process. Specifically, the solution to equation (4) defines a continuous flow map  $\Phi(\mathbf{F}^{nLL}, t)$  originating from the initial state  $\mathbf{F}^{nLL}$ . Owing to the properties of  $f_{\theta}^{\text{LFSP}}$ , this flow is unique. As a result,  $\Phi$  transforms the noisy input  $\mathbf{F}^{nLL}$  into the cleaned output  $\mathbf{F}^{LL}$  along a deterministic trajectory, thereby preventing structural degradation. The inherent smoothness of the mapping ensures effective noise suppression in low-frequency regions, which helps avoid artifacts in the final reconstruction. In summary, by leveraging the NODE framework, the LFSP-ODE approach effectively

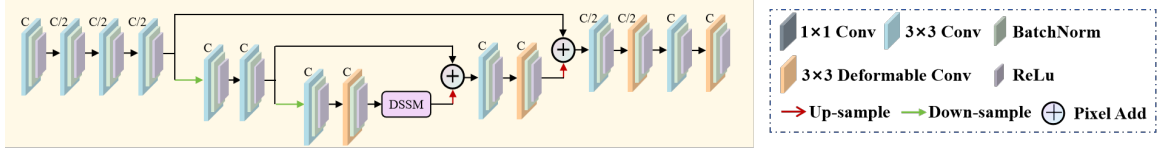


Fig. 6: High-frequency denoising and enhancement (HFDE) module.

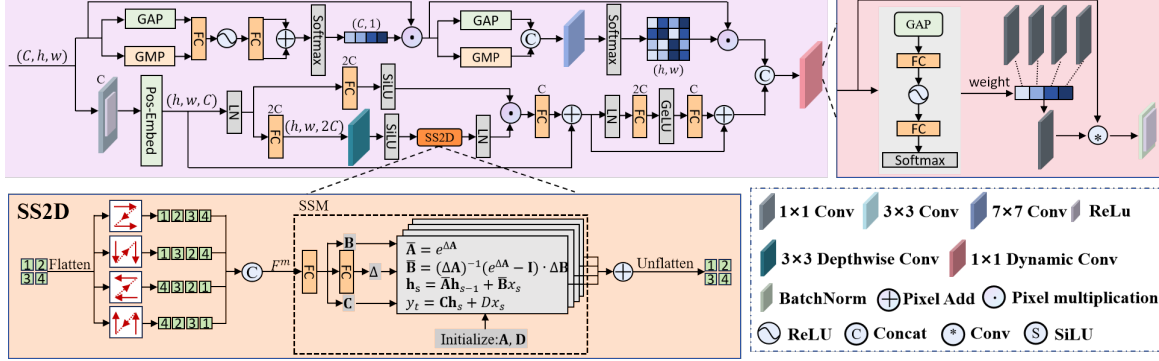


Fig. 7: The framework of the DASS module.

removes noise in low-frequency domains while adaptively preserving structural details.

### C. High-frequency denoising and enhancement module

To reduce noise in the high-frequency components  $\{\mathbf{F}^{\text{NLH}}, \mathbf{F}^{\text{HL}}, \mathbf{F}^{\text{HH}}\}$ , which contain significant sharp edges, strongly scattered isolated point targets, and fine textures, a HFDE module is designed to effectively enhance these structures. And based on difference between these features, we utilize same but unshared HFDE for separate processing. The HFDE adopts an asymmetric U-shaped architecture inspired by U-Net [33], comprising an encoder, a decoder, and a bottleneck module.

Taking the high-frequency component  $\mathbf{F}^{\text{HH}}$  as an example, the process begins by feeding it into a CNN-BN-ReLU block for initial filtering and channel attention squeezing, yielding feature  $\mathbf{F}_0^{\text{e}} \in \mathbb{R}^{\frac{C}{2} \times \frac{H}{2} \times \frac{W}{2}}$ . It is then put into encoder composed of 2 CNN-BN-ReLU-MaxPool layers with downsampling ratio of 2 as follows:

$$\mathbf{F}_i^{\text{e}} = \text{Encoder}(\mathbf{F}_{i-1}^{\text{e}}), \quad i = 1, 2.$$

In the bottleneck stage, it consisted of a CNN-BN-ReLU and a DeforConv-BN-ReLU. Besides, we introduce a DASS module to extract global features and emphasize salient regions:

$$\mathbf{F}_0^{\text{d}} = \text{DASS}(\mathbf{F}_2^{\text{e}}).$$

The decoder adopts an different structures from the encoder. Since the fixed receptive field of traditional CNNs limits their ability to capture complex geometric structures, such as multi-scale shapes and irregular boundaries, we employ deformable convolutions. These allow the network to dynamically adapt the sampling locations of the convolution kernel via learned offsets, enhancing adaptability to geometric variations. The deformable convolution (DeforConv) operation is defined as:

$$y(k_0) = \sum_{k \in R} \omega(k_0) x(k_0 + k + \Delta k),$$

where  $k_0$  is the processing pixel,  $R$  is sampling the regular grid of convolution, and  $\Delta k$  denotes the learned offset. The offset is learned from the preceding feature maps, via additional convolutional layers. Thus, it can adaptively capture the vary of different feature maps. In addition, dense skip connections are incorporated to mitigate information loss. The decoding process is formulated as:

$$\mathbf{F}_i^{\text{d}} = \text{Decoder}(\mathbf{F}_{i-1}^{\text{d}} + \mathbf{F}_{i-1}^{\text{e}}).$$

Finally, two CNN-BN-ReLU with kernel size 3x3 are used to obtain the high-frequency denoising output  $\mathbf{F}^{\text{HH}} \in \mathbb{R}^{C \times \frac{H}{2} \times \frac{W}{2}}$ .

### D. Dynamic attentive state-space fusion module

To effectively preserve structural information, it is essential to extract rich features from both low-frequency and high-frequency components of an image. To this end, we design a Dynamic Attentive State-Space Fusion (DASS) module that adaptively extracts both local and global features for denoising. As illustrated in figure 7, DASS adopts a dual-branch architecture that integrates a local detailed context branch and a global context branch, leveraging their complementary strengths through adaptive fusion. The detail branch incorporates a CBAM block [17], which enhances useful features and structural details through sequential channel and spatial attention. The global branch employs a Mamba-based structure to efficiently capture global contextual information with linear computational complexity.

Given an intermediate feature map  $\mathbf{F}^{\text{m}} \in \mathbb{R}^{C \times H \times W}$ , the detail branch generates a channel attention map  $\mathbf{W}^{\text{cha}} \in \mathbb{R}^{C \times 1 \times 1}$  and a spatial attention map  $\mathbf{W}^{\text{spa}} \in \mathbb{R}^{1 \times H \times W}$  through pooling operations to highlights informative channels and suppresses noise and emphasize spatially important regions, respectively. The output of this branch is computed as:

$$\mathbf{F}^{\text{at}} = \mathbf{W}^{\text{spa}} \odot (\mathbf{W}^{\text{cha}} \odot \mathbf{F}^{\text{m}}),$$

where  $\odot$  denotes element-wise multiplication.

Global feature representation is crucial for reconstructing image structures, yet CNNs are inherently limited by local receptive fields. To overcome this, we integrate a visual state space (VSS) block from VMamba [23] to efficiently model long-range dependencies. The process is formulated as:

$$\begin{aligned}\tilde{\mathbf{F}}^m &= \text{LN}(\text{Conv1} \times 1(\mathbf{F}^m) + \text{Pos-Embed}), \\ \tilde{\mathbf{F}}_1^{\text{VSS}} &= \text{SiLU}(\text{FC}(\tilde{\mathbf{F}}^m)), \\ \tilde{\mathbf{F}}_2^{\text{VSS}} &= \text{LN} \left( \text{SS2D} \left( \sigma(\text{FC}(\text{DWConv}(\tilde{\mathbf{F}}^m))) \right) \right), \\ \tilde{\mathbf{F}}^{\text{VSS}} &= (\tilde{\mathbf{F}}_1^{\text{VSS}} \odot \tilde{\mathbf{F}}_2^{\text{VSS}}) + \tilde{\mathbf{F}}^m, \\ \mathbf{F}^{\text{VSS}} &= \tilde{\mathbf{F}}^{\text{VSS}} + \text{FFN}(\tilde{\mathbf{F}}^{\text{VSS}}).\end{aligned}$$

where LN denotes LayerNorm, and FFN is a feed-forward network composed of two fully-connected (FC) layers and a Gaussian error linear unit. The SS2D mechanism transforms 2D features into sequences through four directional scans, captures global dependencies using state-space models, and then fused through weighted integration to reconstruct a 2D feature map.

Finally, the local detail feature  $\mathbf{F}^{\text{at}}$  and global feature  $\mathbf{F}^{\text{VSS}}$  are adaptively fused using dynamic convolution (DConv). The features are first concatenated to form  $\mathbf{F}^f \in \mathbb{R}^{2C \times H \times W}$ . A soft attention vector  $\alpha \in \mathbb{R}^K$  is generated through global average pooling and fully connected layers:

$$\alpha = \text{Softmax}(\text{FC}(\text{ReLU}(\text{FC}(\text{GAP}(\mathbf{F}^f))))) ,$$

which determines the weights for  $K$  convolutional kernels of size  $k \times k$ . The dynamic kernel and bias are computed as:

$$\mathbf{W} = \sum_{k=1}^K \alpha_k \tilde{\mathbf{W}}_k, \quad \mathbf{b} = \sum_{k=1}^K \alpha_k \tilde{\mathbf{b}}_k.$$

The concatenated feature is then fused as:

$$\tilde{\mathbf{F}}^f = \text{ReLU}(\text{BN}(\mathbf{W} * \mathbf{F}^f + \mathbf{b})) ,$$

where  $*$  denotes the convolution operation.

The overall function of the DASS module can be summarized as:

$$\tilde{\mathbf{F}}^m = \text{DConv1} \times 1([\mathbf{F}^{\text{at}} || \mathbf{F}^{\text{VSS}}]) ,$$

where  $\text{DConv1} \times 1(\cdot)$  denotes dynamic convolution with a  $1 \times 1$  kernel, and  $[\cdot]$  represents concatenation along the channel dimension.

## V. EXPERIMENTS AND RESULTS

### A. Experimental Details

1) *Datasets*: To evaluate the proposed model, experiments are conducted on both synthetic and real SAR images. For synthetic evaluations, we use the UC Merced land-use (UCL) [37] dataset, which consists of images from the USGS National Map Urban Area Imagery. It includes 21 land-use categories, each containing 100 images. From each category, 70 images are randomly selected for training, 15 for validation, and 1 for testing. To further assess texture preservation performance, we also experiment on two texture datasets: the Describable Textures Dataset (DTD) [38] and the Flickr

Material Database (FMD) [39]. The DTD contains 5,640 texture images categorized into 47 human-defined attributes. The FMD includes 1,000 images across 10 material categories. From each category in both DTD and FMD, we select 30 images for training, 10 for validation, and 1 for testing. All images are cropped to  $256 \times 256$  for consistency.

For real SAR image evaluation, we test the proposed SAR-FAH model on three real SAR images acquired by different sensors and with varying numbers of looks, as shown in figure 8. Specifically, figure 8a shows a single-look image from the GaoFen-1 satellite (Air-SAR dataset, 3-m resolution), from which a  $256 \times 256$  region is cropped. Figure 8b is a four-look image from the Capella satellite. Figure 8c is an ICEYE SAR fine-mode image covering Doha International Airport, Qatar, acquired on April 29, 2024.

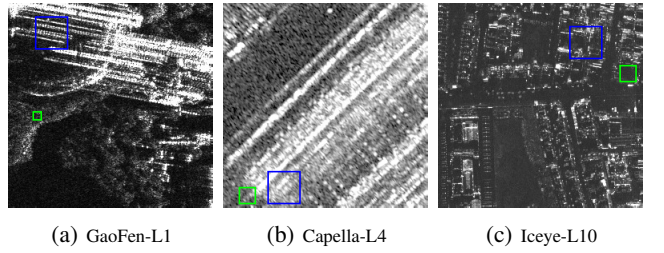


Fig. 8: Real-SAR testing images.

2) *Training setting*: The images are divided into  $128 \times 128$  patches and augmented for training and validation, resulting in a total of 29,400 patches. The model is trained for 20 epochs using the Adam optimizer. The learning rate is set to  $1e-3$  that would be reduced to  $1e-6$  with the cosine annealing. The feature channel  $C$  is set to 128. The torchdiffeq package is employed to solve the NODE with parameters  $T = 1$  and  $N = 4$ . All experiments are implemented using PyTorch 2.2.2 under Python 3.10, and executed on a NVIDIA GeForce GTX 3090 GPU with 24 GB of RAM.

3) *Compared Methods and Quality indexes*: To assess the despeckling performance, we compare the SAR-FAH model with several existing methods: MuLoG-BM3D [40], POTDF [41], SAR-CNN [8], SAR-CAM [6], AGSDNet [11], and SAR-Trans [7], and HTNet [42]. For deep-learning methods, we train on same training dataset and use hyper-parameters as initial lectures.

To evaluate despeckling results on synthetic experiments, we employ five quantitative indices (QIs), including peak signal-to-noise ratio (PSNR), structural similarity (SSIM), mean average error (MAE), gradient-based structural similarity (GSSIM) [43] and image information correlation coefficient (IICC) [44]. Higher PSNR, SSIM, GSSIM, and IICC indicates better performance, while lower MAE means better despeckling results.

Additionally, we use several no-reference QIs to compare the despeckling results on real SAR images, including equivalent number of looks (ENL) [45], mean of image (MoI) [46], and mean of ratio (MoR) [46], edge-preservation degree based on the ratio of average (EPD-ROA) along the horizontal direction (HD) and vertical direction (VD) [47].

The quantitative evaluation results are listed in table I, II,

and III, with the best and second-best performances highlighted in red and blue, respectively.

### B. Results on synthetic UCL dataset

Table I presents the quantitative evaluation results on the UCL dataset. The proposed SAR-FAH model achieves the highest QIs across all noise levels.

TABLE I: The comparisons of QIs for the despeckling performance on 21 synthetic images.

L	Method	PSNR $\uparrow$	SSIM $\uparrow$	MAE $\downarrow$	GSSIM $\uparrow$	IICC $\uparrow$
1	SAR-POTDF [41]	20.52	0.4953	17.6508	0.4465	0.7792
	MuLoG-BM3D [40]	22.07	0.5686	14.8156	0.4991	0.8208
	SAR-CNN [8]	22.98	0.5686	13.4299	0.5367	0.8423
	SAR-CAM [6]	22.68	0.5622	14.1908	0.5131	0.8356
	AGSDNet [48]	23.08	0.5764	13.2322	0.5276	0.8392
	SAR-Trans [7]	<b>23.37</b>	<b>0.6076</b>	<b>12.7642</b>	<b>0.5409</b>	<b>0.8620</b>
	HTNet [42]	23.29	0.5948	12.9315	0.5331	0.8505
4	SAR-FAH	<b>23.61</b>	<b>0.6260</b>	<b>12.2443</b>	<b>0.5540</b>	<b>0.8721</b>
	SAR-POTDF [41]	24.25	0.6567	11.4681	0.5766	0.8862
	MuLoG-BM3D [40]	25.17	0.6984	10.2977	0.6091	0.9101
	SAR-CNN [8]	25.88	0.7060	9.4799	0.6273	0.9148
	SAR-CAM [6]	25.89	<b>0.7295</b>	<b>9.1478</b>	<b>0.6372</b>	0.9254
	AGSDNet [48]	25.86	0.7024	9.4675	0.6194	0.9117
	SAR-Trans [7]	25.94	0.7238	9.4592	0.6306	<b>0.9282</b>
10	HTNet [42]	<b>26.08</b>	0.7234	9.2817	0.6361	0.9259
	SAR-FAH	<b>26.48</b>	<b>0.7446</b>	<b>8.7610</b>	<b>0.6560</b>	<b>0.9351</b>
	SAR-POTDF [41]	26.40	0.7414	9.0798	0.6571	0.9307
	MuLoG-BM3D [40]	27.33	0.7758	8.0149	0.6867	0.9484
	SAR-CNN [8]	28.00	0.7851	<b>7.4381</b>	0.7002	0.9497
	SAR-CAM [6]	<b>28.10</b>	<b>0.7949</b>	7.4348	<b>0.7095</b>	<b>0.9555</b>
	AGSDNet [48]	27.78	0.7764	7.6112	0.6850	0.9467
10	SAR-Trans [7]	27.66	0.7830	7.8026	0.6857	0.9512
	HTNet [42]	28.00	0.7917	7.4624	0.7025	0.9526
	SAR-FAH	<b>28.41</b>	<b>0.8081</b>	<b>7.0470</b>	<b>0.7173</b>	<b>0.9578</b>

TABLE II: The comparisons of QIs for the despeckling performance on 57 synthetic textural images.

L	Method	PSNR $\uparrow$	SSIM $\uparrow$	MAE $\downarrow$	GSSIM $\uparrow$	IICC $\uparrow$
1	SAR-POTDF [41]	20.49	0.4782	20.4881	0.5180	0.7414
	MuLoG-BM3D [40]	22.20	0.5582	15.3374	0.5906	0.7944
	SAR-CNN [8]	23.20	0.5579	13.8903	0.6027	0.8115
	SAR-CAM [6]	23.04	0.5636	14.4586	0.5902	0.8113
	AGSDNet [48]	23.31	0.5651	13.8043	0.6025	0.8085
	SAR-Trans [7]	<b>23.87</b>	<b>0.6071</b>	13.1174	<b>0.6154</b>	<b>0.8353</b>
	HTNet [42]	<b>23.87</b>	0.6038	<b>13.0610</b>	<b>0.6154</b>	0.8295
4	SAR-FAH	<b>23.98</b>	<b>0.6146</b>	<b>12.8600</b>	<b>0.6191</b>	<b>0.8359</b>
	SAR-POTDF [41]	24.59	0.6458	11.7017	0.6376	0.8624
	MuLoG-BM3D [40]	25.27	0.6859	10.8203	0.6703	0.8797
	SAR-CNN [8]	25.99	0.6953	10.1294	0.6818	0.8872
	SAR-CAM [6]	25.84	0.6855	10.5167	0.6693	0.8865
	AGSDNet [48]	25.84	0.6833	10.3166	0.6720	0.8817
	SAR-Trans [7]	25.85	0.7081	10.3923	0.6809	0.8930
10	HTNet [42]	<b>26.34</b>	<b>0.7149</b>	<b>9.8157</b>	<b>0.6872</b>	<b>0.8940</b>
	SAR-FAH	<b>26.59</b>	<b>0.7209</b>	<b>9.5759</b>	<b>0.6912</b>	<b>0.8987</b>
	SAR-POTDF [41]	26.78	0.7302	9.2264	0.7008	0.9075
	MuLoG-BM3D [40]	27.39	0.7585	8.5393	0.7229	0.9162
	SAR-CNN [8]	27.74	0.7640	8.2928	0.7319	0.9195
10	SAR-CAM [6]	28.01	0.7707	8.2424	0.7262	0.9222
	AGSDNet [48]	27.57	0.7509	8.5154	0.7187	0.9145
	SAR-Trans [7]	26.93	0.7629	9.2541	0.7161	0.9191
	HTNet [42]	<b>28.09</b>	<b>0.7817</b>	<b>8.0362</b>	<b>0.7357</b>	<b>0.9248</b>
	SAR-FAH	<b>28.38</b>	<b>0.7891</b>	<b>7.8152</b>	<b>0.7402</b>	<b>0.9282</b>

Visual results on UCL dataset, including farmland, runways, and chaparral, are shown in figure 9. At the first row, for the farmland image with rich textures, it can be observed that except for SAR-Trans based on transformer framework which

can restore part of textures, other models completely blur the farmland texture. However, it is noted that SAR-Trans causes texture distortion. In contrast, the SAR-FAH model preserves more farmland textures without distortion. At the second row, an runways image is illustrated the edges preservations. It can be seen that the compared models not only blur the edges of the road, but also produce artifacts in homogeneous areas. In contrast, the despeckling result of the proposed model have clear edges without artifacts. In addition, for some fine textures and small isolated targets, they cannot be well restored. As shown in the third row, some seaweeds is blurred or with blurred structures, while the SAR-FAS preserve these fined objects. These better performance are attributed to the use of wavelet transform and the design of special processing on different frequency band for despeckling enabling better results on both homogeneous and heterogeneous regions. Especially, the utilization of NODE framework for low-frequency processing provides better protection for image structures.

### C. Results on synthetic textural dataset

The proposed SAR-FAH model decomposes the image into low-frequency and high-frequency components and processes each with specialized denoising strategies to better preserve structural and textural details. To further evaluate its effectiveness in maintaining textures, a dedicated texture dataset comprising 57 categories was constructed, as summarized in table II. Notably, SAR-FAH consistently achieves the best performance across all QIs.

Visual results on composite texture images, comprising banded, lined, braided, and moderate stone patterns, are presented in figure 10. Severe texture degradation is evident in the noisy image, especially in fine structures such as lined and braided regions, which are critical in practical applications like target boundary. These models tend to over-smooth resulting in blurred textural details. As can be seen, due to the lack of separate processing between homogeneous and heterogeneous regions, in these comparative models, both homogeneous regions and heterogeneous regions rich in texture structures have not achieved good recovery. The artifacts, texture blurring, and texture distortion phenomena are evident in the results of other models. Clearly, SAR-FAH exhibits superior texture preservation.

### D. Result on real-SAR images

To evaluate the practical value of SAR despeckling methods, we conducted experiments on real SAR images with varying numbers of looks. In the absence of clean references, performance was assessed using both visual performance and no-reference metrics. As shown in figures 11–13, the proposed SAR-FAH model consistently achieves superior visual results across all datasets. It effectively removes speckle noise while preserving critical structural details such as edges, corners, and textures, significantly outperforming comparison methods, which often suffer from over-smoothing, residual noise, or loss of detail. This balance is attributed to the wavelet-based decomposition and frequency-adaptive processing strategy of SAR-FAH.

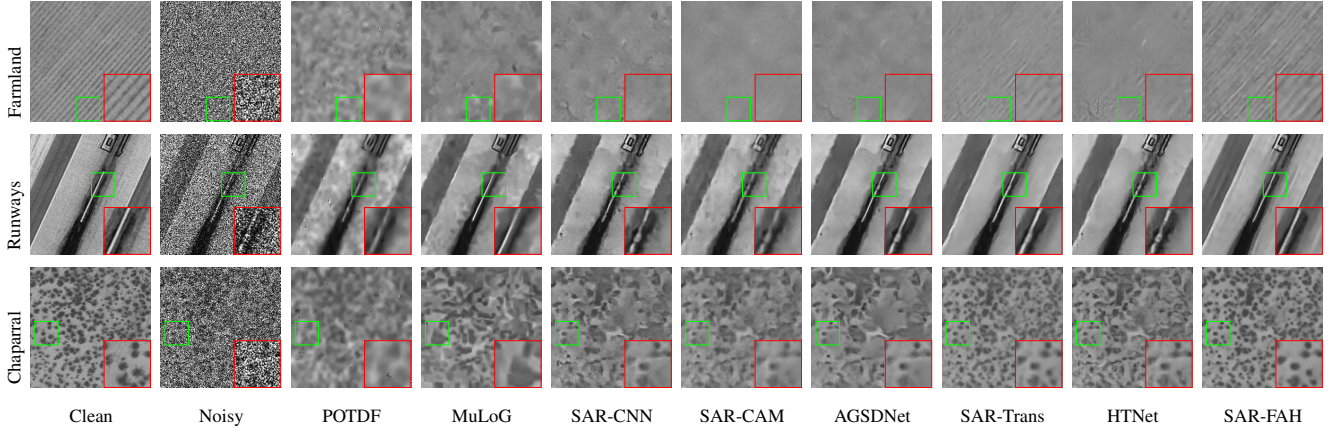


Fig. 9: Despeckling visual results on UCL dataset under noise level of  $L = 1$ .

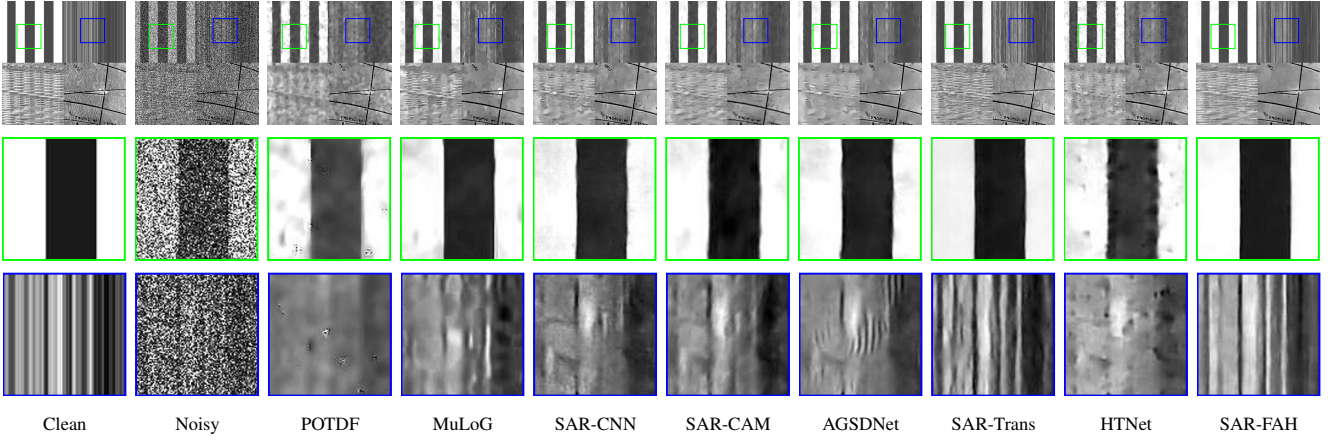


Fig. 10: Despeckling visual results on textural dataset under noise level of  $L = 1$ .

For quantitative evaluation, 4 no-reference QIs are used to evaluate the quality of despeckle images. To analyse the despeckling performance of homogeneous regions, ENL and MoI are calculated in green box of real-SAR images with size of  $10 \times 10$ ,  $20 \times 20$ , and  $20 \times 20$ , respectively. EPD-ROA is calculated to evaluate the edge preservation in heterogeneous regions, which are boxed in blue with size of  $40 \times 40$  as shown in figure 8. Besides, MoR is calculated to determine the mean preservation of real-SAR image to evaluate overall performance.

Quantitative results further confirm the advantages of SAR-FAH. As summarized in table III, it achieves the best or second-best scores across multiple no-reference QIs. Notably, SAR-FAH excels in both homogeneous region smoothing and structural preservation, with MoR values closest to 1, indicating excellent radiometric consistency. These results demonstrate that SAR-FAH robustly balances speckle suppression and detail retention across diverse real SAR scenarios, underscoring its strong practical applicability.

#### E. Ablation study

An ablation study on the UCL dataset analyses the efficiency of main structures of SAR-FAH shown in figure 2. We test on 21 test images to evaluate them on four QIs with learned

parameters to illustrate their despeckling performance and efficiency.

Table IV lists the influence of key modules in the proposed SAR-FAH framework. The DASS module extracts both detailed and global features, which are dynamically fused to enhance structural preservation in both the LFSP-ODE and HFDE modules. When using  $1 \times 1$  convolution to fuse features instead of DCN, it leads to a slight degradation in speckle reduction performance, along with an increase in the number of parameters. Ablation studies further reveal that removing the DASS module from LFSP-ODE, HFDE, or both results in a decline across all QIs, which indicates that the absence of joint local and global feature extraction leads to excessive smoothing and weakened structural retention. Additionally, in the proposed SAR-FAH, we use same but un-shared HFDE to smooth noise in three high-frequency denoising. Experiment shows that using a shared HFDE module fails to fully remove speckle noise. It implies that although high-frequency components exhibit similar noise distributions, they contain distinct structural characteristics that require specialized, non-shared processing modules for effective denoising.

Table V summarizes the impact of the NODE framework, which achieves improved performance and enhanced structural fidelity with fewer parameters. Removing the NODE struc-

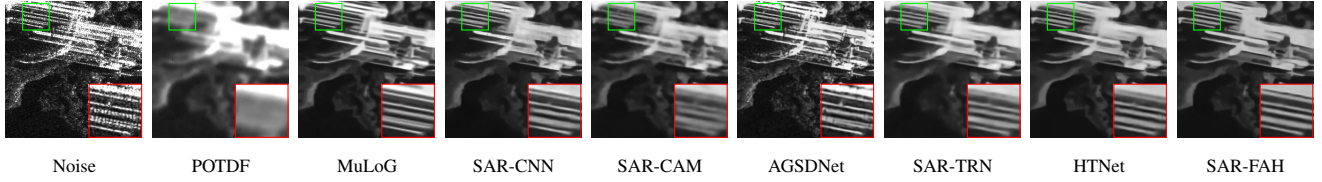


Fig. 11: Despeckling visual results on GaoFen-L1 dataset with a demarcated area zoomed in 2 times for easy comparison.

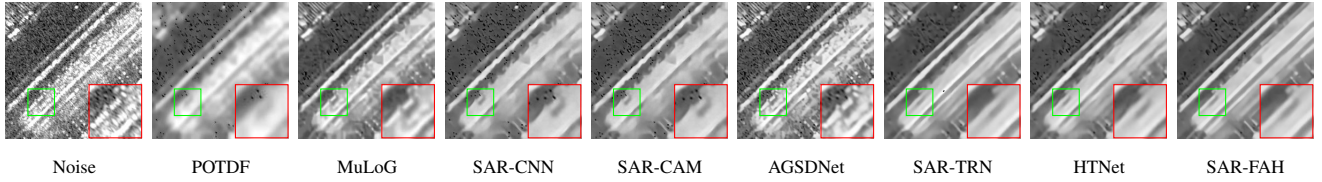


Fig. 12: Despeckling visual results on Capella-L4 dataset with a demarcated area zoomed in 2 times for easy comparison.

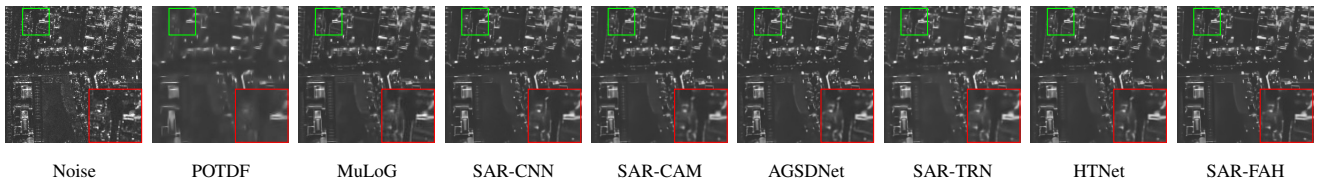


Fig. 13: Despeckling visual results on Iceye-L10 dataset with a demarcated area zoomed in 2 times for easy comparison.

TABLE III: The comparisons of no-reference QIs of the despeckling performance on 3 real-SAR images from different satellites.

Image	Method	ENL↑	MoI↑	EPD-ROA		MoR↑
				HD↑	VD↑	
Best value		$+\infty$	1	1	1	1
GaoFen-L1	AGSDNet	24.52	0.9835	0.8721	0.8454	2.2219
	POTDF	82.58	0.6242	0.8552	0.7465	0.6586
	MuLoG	50.03	0.9734	0.8575	0.7871	0.9593
	SAR-CNN	250.62	0.9685	0.8596	<b>0.7935</b>	<b>0.9747</b>
	SAR-CAM	155.58	1.0188	0.8585	0.7696	0.9683
	SAR-Trans	247.41	0.9407	0.8596	0.7818	0.8911
	HTNet	<b>258.44</b>	<b>1.0116</b>	<b>0.8610</b>	0.7912	0.9679
	SAR-FAH	<b>1213.76</b>	<b>0.9905</b>	<b>0.8611</b>	<b>0.7970</b>	<b>0.9896</b>
Capella-L4	AGSDNet	409.33	0.9819	0.9943	0.9923	1.2849
	POTDF	484.10	0.9008	0.9946	0.9912	0.8977
	MuLoG	420.87	<b>0.9983</b>	0.9941	0.9917	<b>0.9925</b>
	SAR-CNN	2228.79	1.0103	0.9943	0.9921	0.9877
	SAR-CAM	598.46	1.0068	0.9941	0.9913	0.9912
	SAR-Trans	1316.61	0.9888	<b>0.9956</b>	<b>0.9926</b>	0.9885
	HTNet	<b>3142.57</b>	1.0056	0.9951	<b>0.9923</b>	0.9864
	SAR-FAH	<b>2517.38</b>	<b>1.0046</b>	<b>0.9961</b>	0.9921	<b>0.9964</b>
Iceye-L10	AGSDNet	11099.97	0.9920	0.9686	0.9686	1.1064
	POTDF	7709.54	0.9483	0.9633	0.9668	0.9786
	MuLoG	5137.75	0.9959	<b>0.9747</b>	<b>0.9732</b>	1.0049
	SAR-CNN	3880.31	0.9811	0.9692	0.9676	<b>0.9971</b>
	SAR-CAM	18013.44	<b>0.9965</b>	0.9670	0.9673	0.9920
	SAR-Trans	24775.88	0.9303	0.9656	0.9670	0.9366
	HTNet	<b>30466.81</b>	0.9900	0.9667	0.9674	0.9869
	SAR-FAH	<b>25681.02</b>	<b>1.0091</b>	<b>0.9760</b>	<b>0.9697</b>	<b>1.0034</b>

ture from the LFSP-ODE module, while keeping the total parameter count unchanged, leads to significant degradation in structural preservation. Replacing NODE with discrete residual connections of the same depth substantially increases the number of parameters without yielding performance gains. These results demonstrate that the NODE framework in LFSP-ODE effectively contributes to better structural preservation as

TABLE IV: The ablation study of main structure in SAR-FAH.

Method	Parm ↓	PSNR ↑	SSIM ↑	MAE ↓	GSSIM ↑
w/o DCN in DASS	7.40	<b>23.51</b>	<b>0.6198</b>	<b>12.3688</b>	<b>0.5510</b>
w/o DASS in LFSP-ODE	6.92	23.25	0.5963	12.8012	0.5370
w/o DASS in HFDE	6.67	22.87	0.5743	13.3008	0.5293
w/o DASS	<b>6.08</b>	23.40	0.6046	12.5704	0.5409
shared HFDE	<b>3.71</b>	23.44	0.6162	12.5218	0.5473
SAR-FAH	7.32	<b>23.61</b>	<b>0.6260</b>	<b>12.2443</b>	<b>0.5540</b>

TABLE V: The ablation study of NODE framework in LFSP-ODE.

Method	Parm ↓	PSNR ↑	SSIM ↑	MAE ↓	GSSIM ↑
w/o NODE	<b>7.32</b>	23.18	0.5966	12.8905	0.5348
Residual substitution	<b>11.51</b>	<b>23.53</b>	<b>0.6199</b>	<b>12.3318</b>	0.5487
SAR-FAH	<b>7.32</b>	<b>23.61</b>	<b>0.6260</b>	<b>12.2443</b>	<b>0.5540</b>

well as less computational burden.

TABLE VI: The ablation study of DeforConv in HFDE.

Encoder	Decoder	Parm ↓	PSNR ↑	SSIM ↑	MAE ↓	GSSIM ↑
✗	✗	<b>7.23</b>	23.09	0.5920	12.9606	0.5358
✓	✓	7.41	23.48	0.6136	12.4111	<b>0.5473</b>
✓	✗	<b>7.32</b>	<b>23.52</b>	<b>0.6143</b>	<b>12.3487</b>	0.5465
✗	✓	<b>7.32</b>	<b>23.61</b>	<b>0.6260</b>	<b>12.2443</b>	<b>0.5540</b>

Table VI analyses the role of DeforConvs in the asymmetric HFDE module. It is clear that removing DeforConvs from the HFDE leads to a noticeable decline in denoising performance, characterized by reduced effectiveness in high-frequency regions and excessive smoothing of structural details. The asymmetry arises since DeforConvs are used only in the decoder part of the HFDE. When we also integrate them into the encoder, forming a symmetric architecture, denoising performance degrades further and the ability to

preserve high-frequency information is impaired. Similarly, using DeforConvs only in the encoder also yields suboptimal results.

Tables VII and VIII demonstrate the effectiveness of the specialized frequency-domain processing networks LFSP-ODE and HFDE. For evaluation, we constructed two separate datasets: one with limited textures and another with rich textures. Each dataset contains 450 images from 15 categories, and experiments were conducted on 15 representative test images. To accelerate comparison, the feature channel dimension CC was set to 64. As shown in table VII, applying the HFDE to low-frequency denoising causes significant loss of image structure. Conversely, replacing the HFDE with LFSP-ODE for high-frequency denoising results in over-smoothed.

TABLE VII: The ablation study of LFSP-ODE and HFDE for low-frequency bands despeckling.

Method	Parm ↓	PSNR ↑	SSIM ↑	MAE ↓	GSSIM ↑
HFDE + HFDE	1.57	24.41	0.7078	11.1764	0.7807
LFSP-ODE + HFDE	1.90	26.22	0.7491	9.1750	0.8048

TABLE VIII: The ablation study of LFSP-ODE and HFDE for high-frequency bands despeckling.

Method	Parm ↓	PSNR ↑	SSIM ↑	MAE ↓	GSSIM ↑
LFSP-ODE + LFSP-ODE	2.01	20.63	0.4790	18.4267	0.4502
LFSP-ODE + HFDE	1.90	20.66	0.4914	18.2780	0.4586

#### F. Model analysis

1) *Parameter analysis*: The NODE framework is used in LFSP-ODE module to remove noise in low-frequency. In this framework, the hyper-parameter  $N$  in equation (4) is important to control model complexity and impact despeckling performance. As tabulated in table IX, we systematically evaluate its impact on UCL dataset. It is seen that as  $N$  decreases, the testing time increases and the performance comes better firstly and then decreases. The best choice is  $N = 4$  to balance efficiency and performance.

TABLE IX: The parameter analysis of  $N$  in LFSP-ODE.

	Parm ↓ N	PSNR ↑	SSIM ↑	MAE ↓	GSSIM ↑	Time(s) ↓
7.32	1	23.42	0.6152	12.4994	0.5510	1.41
	2	23.55	0.6179	12.3250	0.5498	1.95
	3	23.58	0.6222	12.3159	0.5513	2.64
	4	23.61	0.6260	12.2443	0.5540	3.10
	5	23.60	0.6230	12.2531	0.5505	3.60
	6	23.59	0.6237	12.2684	0.5532	4.27

#### G. Computational efficiency

Balancing computational efficiency with despeckling performance is essential for the practical applicability of SAR despeckling models. As illustrated in figure 14, we compare the denoising effectiveness, parameter count, and GFLOPs of learning-based models. It includes our proposed SAR-FAH-s (with shared HFDE modules), variants SAR-FAH- $i$  (where  $N = i$  in the LFSP-ODE module), and other comparative approaches. Our model also achieves competitive results with

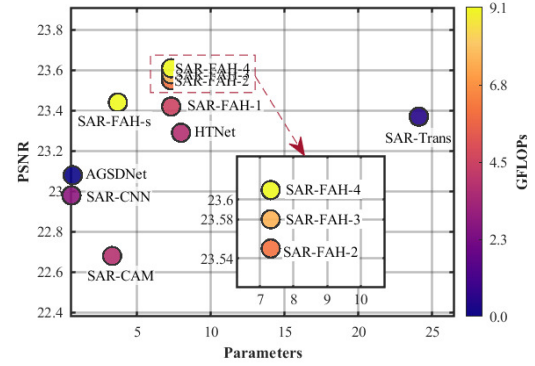


Fig. 14: Efficiency on comparative deep-learning methods, including PSNR, parameters, and GFLOPs, on UCL dataset.

fewer parameters while sharing HFDE parameters. Furthermore, by adjusting the value of  $N$ , we can flexibly control computational complexity. Notably, even when  $N = 1$ , the model maintains strong despeckling performance. These results confirm that the proposed SAR-FAH achieves a favorable balance between despeckling efficacy and computational cost, establishing its strong practical value in despeckling tasks.

## VI. CONCLUSION

We propose a novel SAR-FAH model for SAR despeckling, which employs wavelet transform to decompose the image into different frequency sub-bands, thereby enabling frequency-adaptive processing. For low-frequency homogeneous regions, an LFSP-ODE module based on the neural ODE (NODE) framework is introduced to achieve effective noise suppression in uniform areas while preserving structural integrity without introducing artifacts. In high-frequency sub-bands, an asymmetric U-shaped module derived from U-Net captures multi-scale texture information and incorporates deformable convolutions to extract edges and textures of diverse shapes, thereby maintaining sharp structures and fine details. Furthermore, a DASS module is designed to integrate both attention mechanisms and VMamba structures, dynamically fusing local and global features to enhance overall performance and structural preservation. Extensive experiments are conducted on synthetic SAR datasets, texture datasets, and real SAR images, demonstrating superior performance of the proposed model compared to existing despeckling methods. In particular, it attains the best structural preservation, a benefit attributed to its divide-and-conquer architecture.

## REFERENCES

- [1] V. S. Frost, J. A. Stiles, K. S. Shanmugan, and J. C. Holtzman, “A model for radar images and its application to adaptive digital filtering of multiplicative noise,” *IEEE Transactions on Pattern Analysis and Machine Intelligence*, vol. PAMI-4, no. 2, pp. 157–166, Mar. 1982.
- [2] M. Cheney, “A mathematical tutorial on synthetic aperture radar,” *SIAM Review*, vol. 43, no. 2, pp. 301–312, Jan. 2001.
- [3] S. Luo, L. Tong, and Y. Chen, “A multi-region segmentation method for SAR images based on the multi-texture model with level sets,” *IEEE Transactions on Image Processing*, vol. 27, no. 5, pp. 2560–2574, May 2018.

[4] Z. Wen, Z. Liu, S. Zhang, and Q. Pan, "Rotation awareness based self-supervised learning for SAR target recognition with limited training samples," *IEEE Transactions on Image Processing*, vol. 30, pp. 7266–7279, 2021.

[5] M. Yang, X. Bai, L. Wang, and F. Zhou, "HENC: Hierarchical embedding network with center calibration for few-shot fine-grained SAR target classification," *IEEE Transactions on Image Processing*, vol. 32, pp. 3324–3337, 2023.

[6] J. Ko and S. Lee, "SAR image despeckling using continuous attention module," *IEEE Journal of Selected Topics in Applied Earth Observations and Remote Sensing*, vol. 15, pp. 3–19, 2022.

[7] M. V. Perera, W. G. C. Bandara, J. M. J. Valanarasu, and V. M. Patel, "Transformer-based SAR image despeckling," in *IGARSS 2022 - 2022 IEEE International Geoscience and Remote Sensing Symposium*, Jul. 2022, pp. 751–754.

[8] G. Chierchia, D. Cozzolino, G. Poggi, and L. Verdoliva, "SAR image despeckling through convolutional neural networks," May 2017.

[9] Q. Zhang, Q. Yuan, J. Li, Z. Yang, and X. Ma, "Learning a dilated residual network for SAR image despeckling," *Remote Sensing*, vol. 10, no. 2, p. 196, Jan. 2018.

[10] K. Zhang, W. Zuo, Y. Chen, D. Meng, and L. Zhang, "Beyond a gaussian denoiser: Residual learning of deep cnn for image denoising," *IEEE Transactions on Image Processing*, vol. 26, no. 7, pp. 3142–3155, Jul. 2017.

[11] R. K. Thakur and S. K. Maji, "ADSDNet: Attention and gradient-based SAR denoising network," *IEEE Geoscience and Remote Sensing Letters*, vol. 19, pp. 1–5, 2022.

[12] S. M. Ayyoubzadeh and X. Wu, "High frequency detail accentuation in CNN image restoration," *IEEE Transactions on Image Processing*, vol. 30, pp. 8836–8846, 2021.

[13] A. Frery, H.-J. Muller, C. Yanasse, and S. Sant'Anna, "A model for extremely heterogeneous clutter," *IEEE Transactions on Geoscience and Remote Sensing*, vol. 35, no. 3, pp. 648–659, May 1997.

[14] S. Vitale, G. Ferraioli, and V. Pascazio, "Multi-objective CNN-based algorithm for SAR despeckling," *IEEE Transactions on Geoscience and Remote Sensing*, vol. 59, no. 11, pp. 9336–9349, Nov. 2021.

[15] J. Yu, B. Pan, Z. Yu, C. Li, and X. Wu, "Collaborative optimization for SAR image despeckling with structure preservation," *IEEE Transactions on Geoscience and Remote Sensing*, vol. 63, pp. 1–12, 2025.

[16] P. Wang, H. Zhang, and V. M. Patel, "SAR image despeckling using a convolutional neural network," *IEEE Signal Processing Letters*, vol. 24, no. 12, pp. 1763–1767, Dec. 2017.

[17] S. Woo, J. Park, J.-Y. Lee, and I. S. Kweon, "CBAM: Convolutional block attention module," in *Computer Vision – ECCV 2018*, 2018, vol. 11211, pp. 3–19.

[18] Z. Liu, R. Lai, and J. Guan, "Spatial and transform domain CNN for SAR image despeckling," *IEEE Geoscience and Remote Sensing Letters*, vol. 19, 2022.

[19] S. Liu, L. Zhang, S. Tian, Q. Hu, B. Li, and Y. Zhang, "MFAENet: A multiscale feature adaptive enhancement network for SAR image despeckling," *IEEE Journal of Selected Topics in Applied Earth Observations and Remote Sensing*, vol. 16, pp. 10420–10433, 2023.

[20] R. T. Q. Chen, Y. Rubanova, J. Bettencourt, and D. Duvenaud, "Neural ordinary differential equations," in *Advances in Neural Information Processing Systems 31 (nips 2018)*, 2018.

[21] X. Xie, Y. Wu, H. Ni, and C. He, "NODE-ImgNet: A PDE-informed effective and robust model for image denoising," *Pattern Recognition*, vol. 148, p. 110176, Apr. 2024.

[22] X. Yang, W. Dong, G. Zheng, N. Wang, and X. Gao, "IDENet: An inter-domain equilibrium network for unsupervised cross-domain person re-identification," *IEEE Transactions on Image Processing*, vol. 34, pp. 2133–2146, 2025.

[23] Y. Liu, Y. Tian, Y. Zhao, H. Yu, L. Xie, Y. Wang, Q. Ye, J. Jiao, and Y. Liu, "Vmamba: Visual state space model," Dec. 2024, arXiv:2401.10166.

[24] A. Gu and T. Dao, "Mamba: Linear-time sequence modeling with selective state spaces," 2023, arXiv:2312.00752.

[25] Y. Shi, B. Xia, X. Jin, X. Wang, T. Zhao, X. Xia, X. Xiao, and W. Yang, "VmambaIR: Visual state space model for image restoration," *IEEE Transactions on Circuits and Systems for Video Technology*, vol. 35, no. 6, pp. 5560–5574, Jun. 2025.

[26] Y. Liu, Y. Feng, J. Cheng, H. Zhan, and Z. Zhu, "MambaDiff: Mamba-enhanced diffusion model for 3d medical image segmentation," *IEEE Transactions on Image Processing*, vol. 34, pp. 5761–5775, 2025.

[27] Z. Fu, J. Zhang, L. Wang, L. Xu, H. Laga, Y. Guo, F. Boussaid, and M. Bennamoun, "CompletionMamba: Taming state space model for point cloud completion," *IEEE Transactions on Image Processing*, vol. 34, pp. 5473–5485, 2025.

[28] A. Gu, K. Goel, and C. Ré, "Efficiently modeling long sequences with structured state spaces," Aug. 2022, arXiv:2111.00396.

[29] G. Pechlivanidou and N. Karampetakis, "Zero-order hold discretization of general state space systems with input delay," *IMA Journal of Mathematical Control and Information*, vol. 39, no. 2, pp. 708–730, Jun. 2022.

[30] S. Mallat, "A theory for multiresolution signal decomposition: the wavelet representation," *IEEE Transactions on Pattern Analysis and Machine Intelligence*, vol. 11, no. 7, pp. 674–693, Jul. 1989.

[31] A. Cohen, T. Tiplica, and A. Kobi, "Design of experiments and statistical process control using wavelets analysis," *Control Engineering Practice*, vol. 49, pp. 129–138, Apr. 2016.

[32] P. J. Forrester, "On the gamma difference distribution," *Statistics & Probability Letters*, vol. 211, p. 110136, Aug. 2024.

[33] O. Ronneberger, P. Fischer, and T. Brox, "U-Net: Convolutional networks for biomedical image segmentation," in *Medical Image Computing and Computer-Assisted Intervention – MICCAI 2015*, 2015, vol. 9351, pp. 234–241.

[34] W. E, "A proposal on machine learning via dynamical systems," *Communications in Mathematics and Statistics*, vol. 5, no. 1, pp. 1–11, Mar. 2017.

[35] X. He, Z. Mo, P. Wang, Y. Liu, M. Yang, and J. Cheng, "ODE-inspired network design for single image super-resolution," in *2019 IEEE/CVF Conference on Computer Vision and Pattern Recognition (CVPR)*, Jun. 2019, pp. 1732–1741.

[36] H. Yan, "Towards adverSARial robustness of deep vision algorithms."

[37] Y. Yang and S. Newsam, "Bag-of-visual-words and spatial extensions for land-use classification," in *Proceedings of the 18th SIGSPATIAL International Conference on Advances in Geographic Information Systems*, Nov. 2010, pp. 270–279.

[38] M. Cimpoi, S. Maji, I. Kokkinos, S. Mohamed, and A. Vedaldi, "Describing textures in the wild," in *2014 IEEE Conference on Computer Vision and Pattern Recognition (CVPR)*, 2014, pp. 3606–3613.

[39] L. Sharan, R. Rosenholtz, and E. H. Adelson, "Accuracy and speed of material categorization in real-world images," *Journal of Vision*, vol. 14, no. 9, p. 12, 2014.

[40] C.-A. Deledalle, L. Denis, S. Tabti, and F. Tupin, "MuLoG, or how to apply Gaussian denoisers to multi-channel SAR speckle reduction?" *IEEE Transactions on Image Processing*, vol. 26, no. 9, pp. 4389–4403, Sep. 2017.

[41] B. Xu, Y. Cui, Z. Li, B. Zuo, J. Yang, and J. Song, "Patch ordering-based SAR image despeckling via transform-domain filtering," *IEEE Journal of Selected Topics in Applied Earth Observations and Remote Sensing*, vol. 8, no. 4, pp. 1682–1695, Apr. 2015.

[42] L. Cheng, Z. Guo, Y. Li, and Y. Xing, "Two-stream multiplicative heavy-tail noise despeckling network with truncation loss," *IEEE Transactions on Geoscience and Remote Sensing*, vol. 61, pp. 1–17, 2023.

[43] G.-h. Chen, C.-l. Yang, and S.-l. Xie, "Gradient-based structural similarity for image quality assessment," in *2006 International Conference on Image Processing*, Oct. 2006, pp. 2929–2932.

[44] Z. Wang, A. C. Bovik, and L. G. Lu, "Why is image quality assessment so difficult?" in *2002 IEEE International Conference on Acoustics, Speech, and Signal Processing (ICASSP), Vols. I-IV, Proceedings*, 2002, pp. 3313–3316.

[45] H. Xie, L. Pierce, and F. Ulaby, "SAR speckle reduction using wavelet denoising and markov random field modeling," *IEEE Transactions on Geoscience and Remote Sensing*, vol. 40, no. 10, pp. 2196–2212, Oct. 2002.

[46] G. Di Martino, M. Poderico, G. Poggi, D. Riccio, and L. Verdoliva, "Benchmarking framework for SAR despeckling," *IEEE Transactions on Geoscience and Remote Sensing*, vol. 52, no. 3, pp. 1596–1615, Mar. 2014.

[47] H. Feng, B. Hou, and M. Gong, "SAR image despeckling based on local homogeneous-region segmentation by using pixel-relativity measurement," *IEEE Transactions on Geoscience and Remote Sensing*, vol. 49, no. 7, pp. 2724–2737, Jul. 2011.

[48] Y. Lu, Y. Guo, R. W. Liu, K. T. Chui, and B. B. Gupta, "GradDT: Gradient-guided despeckling transformer for industrial imaging sensors," *IEEE Transactions on Industrial Informatics*, vol. 19, no. 2, pp. 2238–2248, Feb. 2023.